

# SCIENTIFIC REPORTS



OPEN

## Design of Reduction Process of SnO<sub>2</sub> by CH<sub>4</sub> for Efficient Sn Recovery

Hyunwoo Ha<sup>1</sup>, MiYoo<sup>1</sup>, Hyesung An<sup>1</sup>, Kihyun Shin<sup>2,4</sup>, Taeyang Han<sup>1</sup>, Youhan Sohn<sup>1</sup>, Sangyeol Kim<sup>1,3</sup>, Sang-Ro Lee<sup>3</sup>, Jun Hyun Han<sup>1</sup> & Hyun You Kim<sup>1</sup> 

We design a novel method for the CH<sub>4</sub> reduction of SnO<sub>2</sub> for the efficient recovery of Sn from SnO<sub>2</sub> through a study combining theory and experiment. The atomic-level process of CH<sub>4</sub>-SnO<sub>2</sub> interaction and temperature-dependent reduction behavior of SnO<sub>2</sub> were studied with a combination of a multi-scale computational method of thermodynamic simulations and density functional theory (DFT) calculations. We found that CH<sub>4</sub> was a highly efficient and a versatile reducing agent, as the total reducing power of CH<sub>4</sub> originates from the carbon and hydrogen of CH<sub>4</sub>, which sequentially reduce SnO<sub>2</sub>. Moreover, as a result of the CH<sub>4</sub> reduction of SnO<sub>2</sub>, a mixture of CO and H<sub>2</sub> was produced as a gas-phase product (syngas). The relative molar ratio of the produced gas-phase product was controllable by the reduction temperature and the amount of supplied CH<sub>4</sub>. The laboratory-scale experimental study confirmed that CH<sub>4</sub> actively reduces SnO<sub>2</sub>, producing 99.34% high-purity Sn and H<sub>2</sub> and CO. Our results present a novel method for an efficient, green, and economical recycling strategy for Sn with economic value added that is held by the co-produced clean energy source (syngas).

Recovering (extracting) metallic elements from ores has occurred throughout human history<sup>1–5</sup>. Advanced copper and iron smelting technology was required for the development of civilization in history<sup>1–5</sup>. However, although dry- or hydro-smelting technologies are currently used as a core technology in industry, many of these technologies are not green or environmentally friendly<sup>6–13</sup>. The most common dry-smelting or reduction of ores by carbon and flux typically byproducts CO<sub>2</sub> and slag at high temperatures<sup>13–15</sup>. In addition, electrolytic smelting or refining of low-quality metal sources is not cost-effective and produces highly corrosive liquid wastes<sup>6–10,16,17</sup>. During the development of human civilization over the past thousands of years, the most easily mineable and accessible high purity ores have been used first due to economic efficiency. The relative depletion of most economically accessible and mineable ores naturally accompanies the accumulation of used metal wastes; many of these wastes are not appropriately recycled.

Sn (Tin) is a highly demanded industrial material<sup>18–22</sup> that is important for the production of electronics<sup>23–26</sup>, sensors<sup>27–30</sup>, glasses<sup>31–33</sup>, and displays<sup>23,34,35</sup>. The industrial demand of Sn is expected to gradually increase in the near future<sup>20–22</sup> as Sn plays a central role in Pb-free solder<sup>36,37</sup> and transparent electrode<sup>23,34,35</sup>. The current London metal exchange market price of Sn is approximately \$19,900/metric ton as of July 2017<sup>38</sup>, which is more than 3 and 10 times more expensive than Cu and Al, respectively<sup>38</sup>. However, currently, only approximately 30% of the annual industrially consumed Sn is being recovered worldwide<sup>39</sup>, meaning that the remaining 70% of the Sn used is excluded from the recycling process and is eventually wasted. In principle, recovering a metallic element from used metals (wastes and scraps) requires a similar process to the initial ore smelting. To recover high-purity metal from used metal wastes, a combined smelting-electrolytic refining process is typically required, making the recovery process economically nonadvantageous<sup>6,7,9,10,12,13,16</sup>. Such a complicated recovery process weakens the economic driving force for the recovery of metals, such as Sn, which is consumed heavily worldwide.

<sup>1</sup>Department of Materials Science and Engineering, Chungnam National University 99 Daehak-ro, Yuseong-gu, Daejeon, 34134, Republic of Korea. <sup>2</sup>Department of Materials Science and Engineering, KAIST, 291 Daehak-ro, Yuseong-gu, Daejeon, 34141, Korea. <sup>3</sup>A1 Engineering Co., Ltd., 80-19 Yulchonsandan 1-ro, Haeryong-myeon, Suncheon-si, Jeollanam-do, 58034, Republic of Korea. <sup>4</sup>Present address: Department of Chemistry and the Institute for Computational Engineering and Sciences, University of Texas at Austin, Austin, TX, USA. Hyunwoo Ha, MiYoo and Hyesung An contributed equally to this work. Correspondence and requests for materials should be addressed to J.H.H. (email: [jghan@cnu.ac.kr](mailto:jghan@cnu.ac.kr)) or H.Y.K. (email: [kimhy@cnu.ac.kr](mailto:kimhy@cnu.ac.kr))

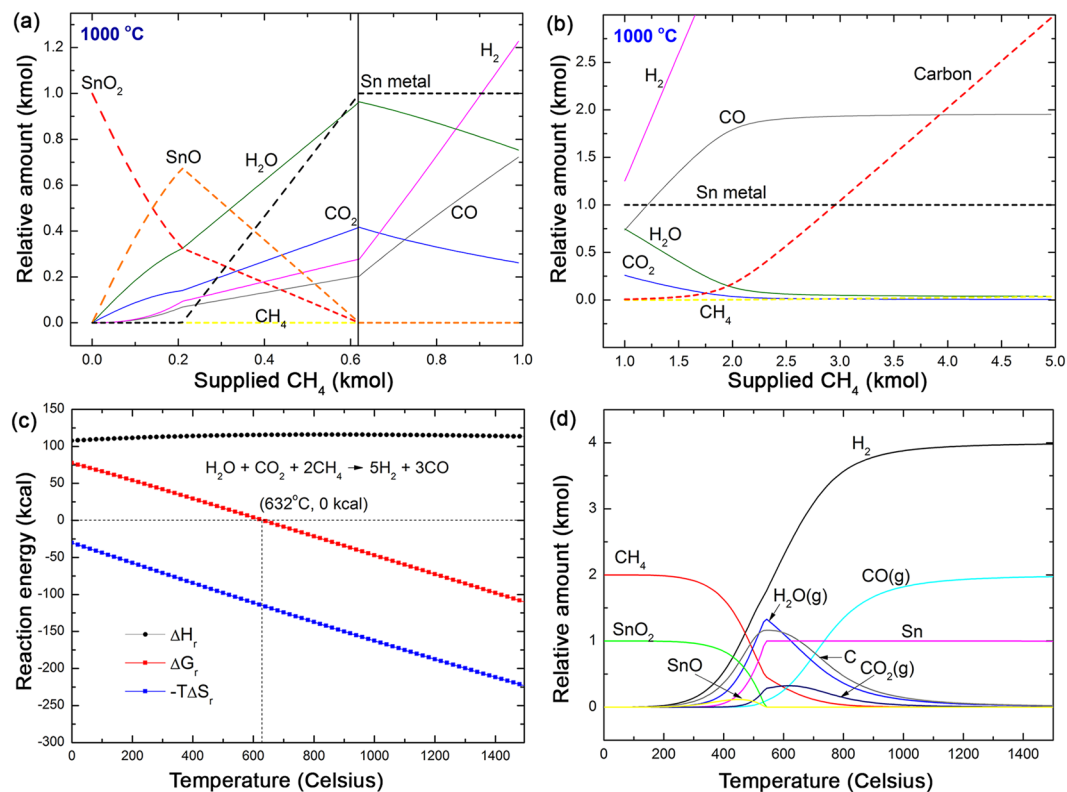


**Figure 1.** Theoretical prediction of the MR of  $\text{SnO}_2$ . **(a,b)** Equilibrium concentration of the mixture of one kmole of  $\text{SnO}_2$  and  $n \cdot \text{CH}_4$  ( $n = 0 \sim 5$ , continuously increasing by a step of 0.01 kmole) at  $1000^\circ\text{C}$  as a function of the amount of supplied  $\text{CH}_4$ . **(a)**  $0 \leq n \leq 1.0$ , **(b)** between  $\text{CH}_4$  and the pre-produced gas-phase products occur as the R ratio exceeds 0.62. **(c)** Temperature dependent reaction energies of two sets of mixtures of gas-phase molecules. The red solid symbols represent the reaction Gibbs free energy,  $\Delta G_r$ , for  $\text{H}_2\text{O} + \text{CO}_2 + 2\text{CH}_4 \rightarrow 5\text{H}_2 + 3\text{CO}$ . The gas phase reaction becomes thermodynamically driven at above  $632^\circ\text{C}$ . **(d)** Temperature dependent equilibrium relative concentration of a  $\text{SnO}_2$ - $\text{CH}_4$  mixture. The initial R value was set to 2.0. Theoretical maximum recovery of Sn was achieved at approximately  $550^\circ\text{C}$ . Although the solid-state reduction of  $\text{SnO}_2$  to Sn was completed at approximately  $1000^\circ\text{C}$ , the relative concentration of the gas-phase products varies as a function of temperature and converges at approximately  $1000^\circ\text{C}$ .

Hydrogen or methane have been utilized as a reducing agent for metal oxides<sup>40–47</sup>. For example, methane reduction (MR)<sup>41,46</sup> or hydrogen reduction of  $\text{ZnO}$ <sup>44,48</sup> was proposed to overcome environmental or economical disadvantages of conventional dry-smelting or recovery techniques. To the best of our knowledge, there are few previous reports on the MR of  $\text{SnO}_2$ . Eroglu and coworkers thermodynamically studied and experimentally demonstrated the feasibility of MR of  $\text{SnO}_2$  method<sup>42</sup>. They also utilized methane as a reducing agent of various metal oxides<sup>43,45,49</sup> confirming the strong reducing power of methane. However, detailed atomic scale understanding of MR of  $\text{SnO}_2$ , which is necessary for optimization of the MR reduction method, is scarce.

In this work, considering the findings of previous studies and combining the widely applied methane dry reforming ( $\text{CH}_4 + \text{CO}_2 \rightarrow 2\text{CO} + 2\text{H}_2$ )<sup>50–53</sup> and the conventional reduction of Sn oxides by carbon ( $\text{SnO}_x + \text{C} \rightarrow \text{Sn} + \text{CO}_x$ ), we study a novel, environmentally friendly MR method of  $\text{SnO}_2$ . We hypothesized that carbon and hydrogen from methane independently and actively reduce  $\text{SnO}_2$ , making the reduction process highly efficient. Moreover, because our MR method utilizes methane and  $\text{SnO}_2$  as a reducer and an oxidizer, respectively, the final gas-phase product naturally involves  $\text{H}_2$  and  $\text{CO}$ . The mixture of  $\text{H}_2$  and  $\text{CO}$ , syngas, can be utilized as a feedstock for further Fisher-Tropsch synthesis<sup>50–53</sup> improving the economic accessibility of our method. Thermodynamic simulations confirmed the availability of the MR of  $\text{SnO}_2$  and deduced the optimal operation conditions for efficient Sn recovery and syngas ( $\text{H}_2 + \text{CO}$ ) production. Density functional theory (DFT) calculations revealed the atomic-level understanding of the process. Subsequent experiments demonstrated that the MR method is very promising for economic and environmentally friendly Sn recovery from  $\text{SnO}_x$ -containing industrial wastes.

## Results

**Theoretical prediction of  $\text{CH}_4$  reduction of  $\text{SnO}_2$ .** Figure 1a and b present the equilibrium concentrations of the mixture for a kmole of  $\text{SnO}_2$  and  $n \cdot \text{CH}_4$  ( $n = 0 \sim 5$ , continuously increasing by a step of 0.01 kmole) at  $1000^\circ\text{C}$  as a function of the amount of supplied  $\text{CH}_4$ . These diagrams were designed to phenomenologically describe the continuous reduction process that occurs inside the reduction furnace in which a certain amount of  $\text{SnO}_2$  is exposed to a stream of  $\text{CH}_4$ . In the early phase of reduction, as the amount of supplied  $\text{CH}_4$

increases, SnO<sub>2</sub> was gradually reduced to SnO rather than completely reduced to Sn. At less than R = 0.21 (R = amount of supplied CH<sub>4</sub>/amount of initial SnO<sub>2</sub> = 0.21), all the decreasing amount of SnO<sub>2</sub> was reduced to SnO (Fig. 1a). In this early phase, the main gas-phase product was H<sub>2</sub>O.

As the amount of supplied CH<sub>4</sub> exceeded R = 0.21, SnO<sub>2</sub> and SnO both began to decrease producing the fully reduced metallic Sn (Fig. 1a). At an equilibrium condition, the supplied SnO<sub>2</sub> can be completely reduced to metallic Sn at R = 0.62. Interestingly, even up to R = 0.62, H<sub>2</sub>O was the main gas-phase product. At R = 0.62, almost half the total supplied oxygen content from SnO<sub>2</sub> was taken up by hydrogen (H<sub>2</sub>O), and the other half formed CO<sub>2</sub> and CO. In the early phase of reduction at less than R = 0.62, the hydrogen and carbon from CH<sub>4</sub> were independently acting as reducing agents. The solid-state reduction of SnO<sub>2</sub> to SnO and Sn by CH<sub>4</sub> was completed at R = 0.62. Up to this point, the amount of SnO<sub>2</sub> and SnO was gradually decreasing and was finally reduced to metallic Sn.

As the R ratio exceeded 0.62, the gas-phase reactions occurred between the excess CH<sub>4</sub> and the pre-existing H<sub>2</sub>, CO, O<sub>2</sub>, and H<sub>2</sub>O in an oxygen-depleted condition (Fig. 1b). All the oxygen from the SnO<sub>2</sub> was already consumed by the hydrogen or carbon. The temperature dependent reaction Gibbs free energy, ΔG<sub>r</sub>, estimated for the reaction H<sub>2</sub>O + CO<sub>2</sub> + 2CH<sub>4</sub> → 5H<sub>2</sub> + 3CO, show that ΔG<sub>r</sub> becomes negative over at above 632 °C (Fig. 1c). A negative ΔG<sub>r</sub> predicts that if CH<sub>4</sub> is continuously supplied to the system over the equilibrium amount for complete solid-state SnO<sub>2</sub> reduction to Sn (R = 0.62), the formation of H<sub>2</sub> and CO becomes thermodynamically preferred at high temperature. As a result of this gas-phase reaction, a mixture of pre-existing CO<sub>2</sub> and H<sub>2</sub>O and excessively supplied CH<sub>4</sub> was converted to H<sub>2</sub> and CO at a high temperature (1,000 °C) (Fig. 1b and c).

Figure 1d shows the temperature dependent equilibrium composition map of a mixture of SnO<sub>2</sub> and CH<sub>4</sub> with R = 2.0. This R value was the critical point where the gas-phase reaction described in Fig. 1c was almost completed. The MR of SnO<sub>2</sub> begins at approximately 300 °C. In the temperature range between 300 °C and 550 °C, the sequential solid-state reduction of SnO<sub>2</sub> to SnO and Sn was completed. As predicted in Fig. 1a and b, the amount of H<sub>2</sub>O, CO<sub>2</sub>, and solid-state carbon produced were rapidly increased in this temperature range. At greater than 550 °C, the gas-phase reaction described in Fig. 1c drives a redistribution of the gas-phase products. Because R = 2.0 is generally the condition with excess CH<sub>4</sub>, a mixture of CH<sub>4</sub>, H<sub>2</sub>O, and CO<sub>2</sub> naturally transforms to H<sub>2</sub> and CO. Moreover, solid-state carbon began to appear even in the initial phase of the solid-state reduction process due to the presence of excess CH<sub>4</sub> in the reduction system. However, this carbon was also decreasing at temperatures greater than 550 °C at which the solid-state reduction is completed and the gas-phase reaction begins. At approximately 1000 °C, the entire gas-phase product was transformed to a mixture of H<sub>2</sub> and CO, increasing the H<sub>2</sub>/CO ratio up to 2.15.

The molecular level process of SnO<sub>2</sub>-CH<sub>4</sub> interaction was studied using DFT calculations. The DFT-calculated binding processes of CH<sub>4</sub> on the (100) and (110) facets of the rutile-SnO<sub>2</sub> show that SnO<sub>2</sub> dissociatively binds CH<sub>4</sub>, producing a lattice oxygen-bound methyl group (O-CH<sub>3</sub><sup>\*</sup>) and a surface hydroxyl (-OH<sup>\*</sup>) (S0 of Fig. 2a and b).

On SnO<sub>2</sub>(100) surface (Fig. 2a), the energetics shows that the direct production of H<sub>2</sub>O from O-CH<sub>3</sub><sup>\*</sup> and -OH<sup>\*</sup> is highly endothermic (ΔE = 1.23 eV) and requires high energy barrier (ΔE<sub>b1</sub> = 1.52 eV, a panel below the S0 of Fig. 2a). On the other hand, further dehydrogenation of O-CH<sub>3</sub><sup>\*</sup> coupled with the formation of additional -OH<sup>\*</sup> is more energetically preferred (S1 of Fig. 2a, ΔE = 0.51 eV and ΔE<sub>b2</sub> = 1.02 eV). We found that, from two separated -OH<sup>\*</sup> groups, the formation of H<sub>2</sub>O molecule is energetically preferred (S2 of Fig. 2) to the H<sub>2</sub> formation (see a panel below S1 of Fig. 2a, ΔE = 1.83 eV) which is again highly endothermic. The desorption of water from the S2 requires only 0.37 eV (see S3 of Fig. 2a). However, further dehydrogenation of O-CH<sub>2</sub><sup>\*</sup> group is endothermic and requires high barrier of 1.12 eV (S4 of Fig. 2a, ΔE<sub>b3</sub> = 1.12 eV). Once a O-CH<sub>2</sub><sup>\*</sup> acetylene group is dissociated, H<sub>2</sub>O and CO or CO<sub>2</sub> production follows. Particularly, the preferred formation of H<sub>2</sub>O is thermodynamically and kinetically favored to the formation of H<sub>2</sub>, confirming the trend in Fig. 1a. Another interesting feature is that a CO molecule was spontaneously formed upon dehydrogenation of a O-CH<sup>\*</sup> group, as presented in S4 and S5 of Fig. 2a. We also found that this CO molecule directly attacks the surface and be transformed to CO<sub>2</sub> with ΔE of -1.61 eV (S7, Fig. 2a). The processes presented in S5 to S7 suggest that solid carbon could directly reduce SnO<sub>2</sub>. However, as the case of carbon coking generally observed in CH<sub>4</sub> reforming catalysis<sup>50-53</sup>, sudden deposition of solid carbon may block the surface of SnO<sub>2</sub>. However, considering that solid carbon would float on the surface of reduced molten Sn, coking would not be a severe issue in MR of SnO<sub>2</sub>.

An almost identical reduction process was observed on SnO<sub>2</sub>(110) (Fig. 2b). The notable difference is that the first O-CH<sub>3</sub><sup>\*</sup> dehydrogenation on SnO<sub>2</sub>(110) is relatively slow compared to that on SnO<sub>2</sub>(100). Dissociation of a O-CH<sub>2</sub><sup>\*</sup> described in S3 and S4 is energetically and kinetically similar with that on SnO<sub>2</sub>(100). Most importantly, SnO<sub>2</sub>(110) surface provides the easier H<sub>2</sub>O desorption pathways as presented in S2 and S3 (ΔE = 0.11 eV) and S5 and S6 (ΔE = 0.13 eV). Because several high-index facets could coexist on the surface of SnO<sub>2</sub> particles or powders, we believe that our DFT-generated SnO<sub>2</sub> reduction pathways would proceed in a bi-functional or a multi-functional manner: Dissociation of a O-CH<sub>3</sub><sup>\*</sup> or a O-CH<sub>2</sub><sup>\*</sup> groups and formation and desorption of H<sub>2</sub>O could occur in a different local area of SnO<sub>2</sub>.

From the molecular structure points, the carbon from CH<sub>4</sub> cannot aggressively reduce SnO<sub>2</sub> in the early phase of reduction. The hydrogen atoms of CH<sub>4</sub> reduce Sn oxides first, and the carbon from CH<sub>4</sub> subsequently reduces the Sn oxides.

CH<sub>4</sub> reforming of CO<sub>2</sub> (dry reforming, CH<sub>4</sub> + CO<sub>2</sub> → 2H<sub>2</sub> + 2CO) and CH<sub>4</sub> steam reforming (CH<sub>4</sub> + H<sub>2</sub>O → 3H<sub>2</sub> + CO) have been applied to produce a mixture of CO and H<sub>2</sub>, which is a feedstock for Fisher-Tropsch synthesis. In general, the molar ratio of H<sub>2</sub> and CO in the CH<sub>4</sub> reforming product gas varies between 1 (dry reforming) and 3 (steam reforming)<sup>12,21,39,50</sup>. In Fig. 1a, at less than R = 0.62, H<sub>2</sub> and CO were minority gas-phase products. However, as SnO<sub>2</sub> and SnO are consumed and the gas-phase reactions occur in oxygen-depleted condition between CH<sub>4</sub> and pre-produced gas-phase molecules, the H<sub>2</sub>/CO ratio rapidly increases as a function of the amount of supplied CH<sub>4</sub>. The rapid increase of the H<sub>2</sub>/CO ratio is

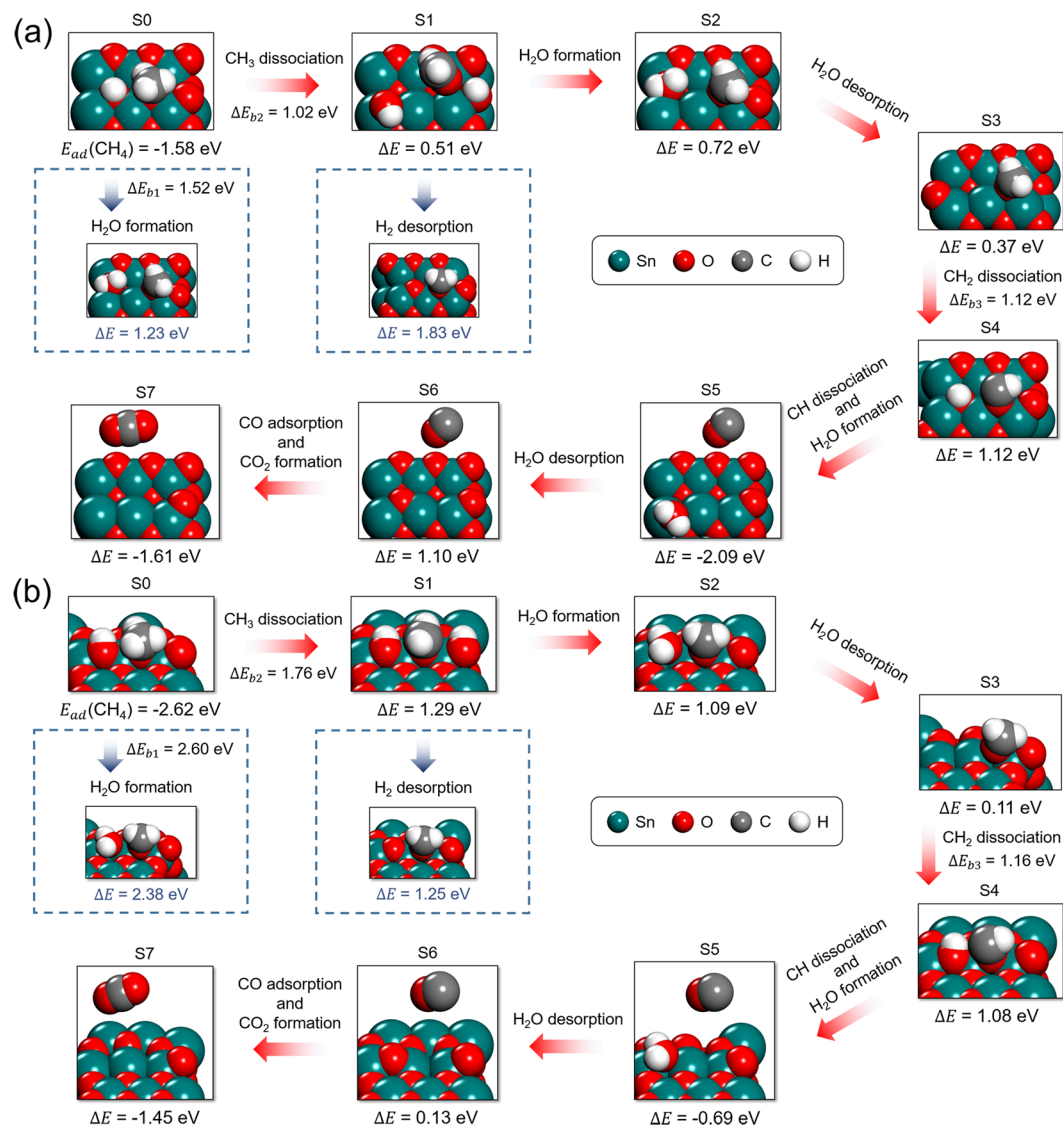


**Figure 2.** Energetics of SnO<sub>2</sub> reduction by surface-bound CH<sub>4</sub>. **(a)** SnO<sub>2</sub> (100) surface. **(b)** SnO<sub>2</sub> (110) surface. On both SnO<sub>2</sub> facets, formation of H<sub>2</sub>O was energetically preferred to H<sub>2</sub>. The red arrows present the preferred reaction pathway.  $E_{ad}(CH_4)$  represents the adsorption energy of CH<sub>4</sub> on the SnO<sub>2</sub> surfaces.  $\Delta E$  of each step represents the energetic state of the current state relative to the previous state. For example,  $\Delta E = 0.51$  eV of S1 in **(a)** means that 0.51 eV of energy is required for CH<sub>3</sub> dissociation from S0 to S1.

phenomenologically feasible because excess CH<sub>4</sub> supplies H, which enters into the system. Moreover, the negative  $\Delta G_r$  also drives the release of H atoms from H<sub>2</sub>O molecules in the form of H<sub>2</sub> molecules.

Typically, CH<sub>4</sub> dry reforming operates at high temperatures above 500 °C and is catalyzed by the transition metal or novel metal catalysts<sup>54,55</sup>. It is not clear whether molten liquid Sn in our system catalyzes the reaction described in Fig. 1c. A recent report by Wetzel and coworkers showed that molten Sn facilitates the thermal dissociation of CH<sub>4</sub> and thus the formation of solid-state carbon and H<sub>2</sub><sup>56,57</sup>. Considering that solid-state carbon and H<sub>2</sub> were increasingly accumulating at greater than R = 2.0 (Fig. 1b), CH<sub>4</sub> dissociation by molten Sn may be attributed to the rapid H<sub>2</sub> and solid carbon formation.

Thermodynamic simulation results presented in Fig. 3 show that the rate of the gas phase reaction,  $H_2O + CO_2 + 2CH_4 \rightarrow 5H_2 + 3CO$ , does not critically affected by the presence of metallic Sn (or molten Sn, Fig. 3a and b). On the other hand, the addition of metallic Sn promotes thermal decomposition of CH<sub>4</sub> (Fig. 3c and d). At 550 °C, at which the solid-state reduction is completed, the amount of decomposed CH<sub>4</sub> was increased by 19.8 % in the presence of metallic Sn. This result theoretically reproduces the recent experimental findings reported by Wetzel and coworkers<sup>56,57</sup>.

Although the MR of SnO<sub>2</sub> is not a catalytic reaction, a reasonable amount of the H<sub>2</sub> and CO mixture was acquired as a byproduct as the R value exceeded 0.62. At approximately R = 2.0, H<sub>2</sub>O and CO<sub>2</sub> in the system began to be depleted. All the oxygen in the system was taken by carbon-forming CO molecules, and the excess carbon

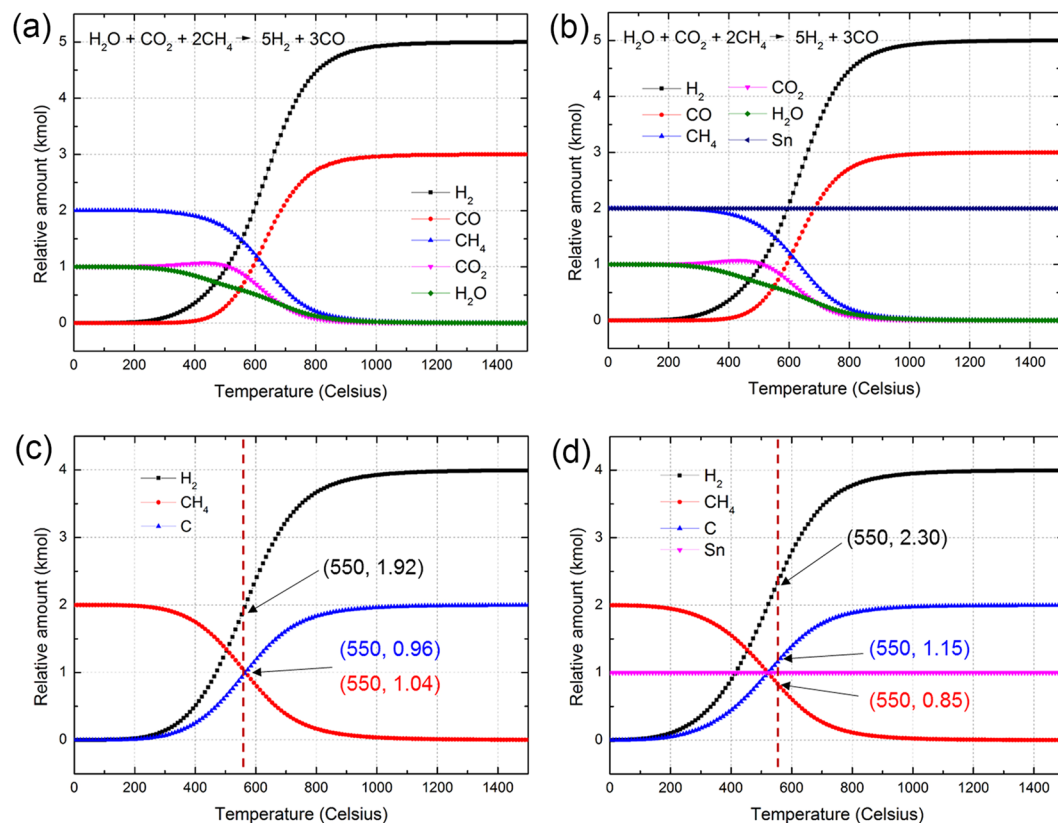


**Figure 3.** Thermodynamic simulations of the Sn effect on the gas phase reactions. **(a,b)** Temperature dependent equilibrium concentration of gas phase species without Sn **(a)** and with Sn **(b)**. The presence of metallic Sn does not significantly affect the transformation of  $\text{H}_2\text{O} + \text{CO}_2 + 2\text{CH}_4 \rightarrow 5\text{H}_2 + 3\text{CO}$ . **(c,d)** Temperature dependent concentration of  $\text{CH}_4$  and decomposed products;  $\text{H}_2$  and C, without Sn **(c)** and with Sn **(d)**. Metallic Sn accelerates thermal decomposition of  $\text{CH}_4$  into C and  $\text{H}_2$ . The numbers in the parentheses represent the equilibrium concentration of  $\text{CH}_4$ , C, and  $\text{H}_2$  at  $550^\circ\text{C}$ , at which theoretical maximum recovery of Sn was achieved (see Fig. 1d).

from the  $\text{CH}_4$  was transformed to solid carbon. During this stage, the increasing  $\text{H}_2$  content in the system was entirely from the excess  $\text{CH}_4$ .

**Experimental confirmation of  $\text{CH}_4$  reduction of  $\text{SnO}_2$ .** To verify the feasibility of the theoretically proposed concept of the MR of  $\text{SnO}_2$ , we constructed a laboratory-scale experimental reduction furnace (Figure S1) with continuously flowing  $\text{CH}_4$  over the exposed  $\text{SnO}_2$  powders. Figure 3a and b show the before and after images of an aluminum boat initially loaded with 25 g of  $\text{SnO}_2$  and reduced at  $1000^\circ\text{C}$  with supplied  $\text{CH}_4$ . Ar-balanced  $\text{CH}_4$  gas continuously flowed through a quartz tube furnace for a total reduction time of 1 hour (flow rate of  $\text{CH}_4$ : 250 sccm). Inevitably, a large portion of supplied  $\text{CH}_4$  bypasses  $\text{SnO}_2$  powders, being decomposed eventually into C and  $\text{H}_2$ . Of course, an industrially applicable furnace should be designed to minimize the amount of bypassing  $\text{CH}_4$ .

The presence of a glittering metallic phase in Fig. 3b shows that  $\text{SnO}_2$  was reduced to metallic Sn. An XRD analysis confirmed that initial  $\text{SnO}_2$  was reduced to crystalline  $\beta$ -Sn (Fig. 4c). A data set tabulated in Table 1 shows the high purity of the Sn reduced by  $\text{CH}_4$ . It is remarkable that almost 80% of the supplied Sn was recovered (Fig. 4) even in the test batch experiment. Additionally, the reduced Sn had a high purity of 99.34% (ICP-analyzed). The concentration of the gas phase products shows a high  $\text{H}_2/\text{CO}$  ratio of 5.99, which exceeds the theoretical maximum of conventional  $\text{CH}_4$  reforming (Table 2). As we mentioned above, thermally decomposed bypassing  $\text{CH}_4$  contributes to the high  $\text{H}_2/\text{CO}$  ratio. The thermodynamically predicted  $\text{H}_2/\text{CO}$  ratio in our reaction condition is about 2.30, which is close to that of convenient syngas for fuel production<sup>58</sup>.

## Discussion

Development of an environmentally friendly and economically accessible reduction technology for low-quality used metal wastes is key for the sustainable use of limited resources. The MR of  $\text{SnO}_2$  method is environmentally and economically novel compared to the conventional dry- and wet-reduction methods, as the MR of  $\text{SnO}_2$  does not involve the use of solid reducing agents and liquid-phase acidic electrolytes. The efficiency of the MR of  $\text{SnO}_2$  was theoretically proposed and experimentally verified. Moreover, because the MR of  $\text{SnO}_2$  occurs at the solid-gas phase interface, the reaction can be more effective than solid-solid interactions of conventional dry reduction.

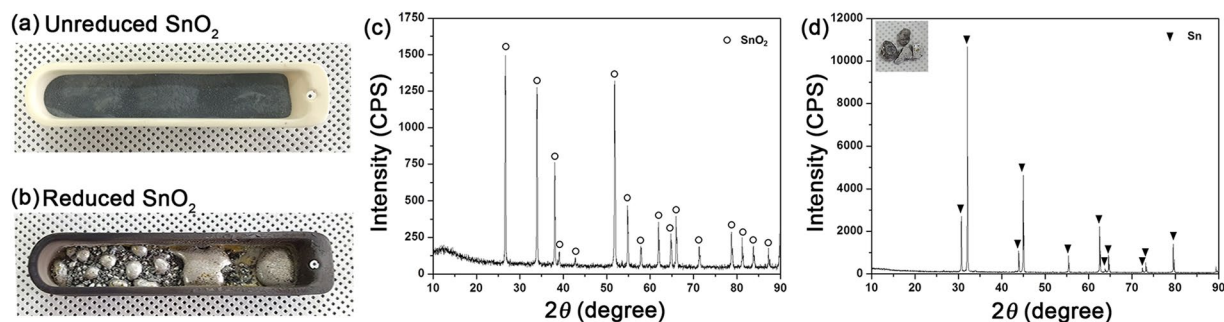


**Figure 4.** Experimental results of the  $\text{CH}_4$  reduction of  $\text{SnO}_2$ . Photos of unreduced  $\text{SnO}_2$  powder (a) and  $\text{CH}_4$  reduced  $\text{SnO}_2$  (b). (c) and (d) show XRD spectra of unreduced  $\text{SnO}_2$  and reduced  $\text{SnO}_2$ , respectively. XRD pattern in (d) demonstrates a typical case of  $\beta$ -Sn. The recovery rate of Sn was 79.9 %.

| Element            | Sn    | Sb   | As    | Cu   | Fe   |
|--------------------|-------|------|-------|------|------|
| Composition (at %) | 99.34 | 0.13 | 0.001 | 0.49 | 0.04 |

**Table 1.** ICP-analyzed composition of the reduced Sn.

| Molecule          | $\text{H}_2^b$ | $\text{CO}^b$ | $\text{CO}_2$ | $\text{CH}_4$ |
|-------------------|----------------|---------------|---------------|---------------|
| Concentration (%) | 83.9           | 14.0          | 1.7           | 0.4           |

**Table 2.** Molecular concentration of the gas-phase product from the  $\text{CH}_4$  reduction of  $\text{SnO}_2$  analyzed using gas chromatography<sup>a</sup>. <sup>a</sup> $\text{H}_2\text{O}$  was not analyzed. <sup>b</sup> $\text{H}_2/\text{CO} = 5.99$ .

$\text{CH}_4$  is a quite efficient and versatile reducing agent because the carbon and hydrogen of  $\text{CH}_4$  sequentially reduce  $\text{SnO}_2$  and produce various gas-phase products. This versatility of  $\text{CH}_4$  is highly beneficial for practical uses because the two most representative reducing agents, hydrogen and carbon, contribute to the total reducing power of  $\text{CH}_4$ .

The theoretical interpretation predicts that as a result of a gas-phase reaction between excess  $\text{CH}_4$  and pre-produced  $\text{H}_2\text{O}$  and  $\text{CO}_2$ , the carbon and hydrogen in the reduction system are eventually transferred to  $\text{CO}$  and  $\text{H}_2$ . Our theory-experimental combination study found that the  $\text{H}_2/\text{CO}$  ratio in the gas-phase product is adjustable by controlling the amount of supplied  $\text{CH}_4$  and the temperature. Gas-phase reactions between initial gas-phase products of  $\text{SnO}_2$  and  $\text{CH}_4$  interaction should be considered for optimization of  $\text{H}_2/\text{CO}$  ratio. The economic value added of the MR of  $\text{SnO}_2$  increases as long as syngas is producible as a byproduct. Industrially attractable quality of syngas could be produced through further optimization of the reaction temperature, total reaction time, and supplied  $\text{SnO}_2/\text{CH}_4$  ratio.

In addition, our preliminary calculations show that butane or propane also vigorously reduce  $\text{SnO}_2$ . For instance, we found that propane completed the  $\text{SnO}_2$  reduction at around  $400^\circ\text{C}$ . Considering that the MR of  $\text{SnO}_2$  was finished at  $550^\circ\text{C}$  (see Fig. 1c), this preliminary data predicts that the propane reduction of  $\text{SnO}_2$  would be economically more effective than the MR of  $\text{SnO}_2$ . If their reducing power is verified by experiment, more economically accessible liquid natural gas or liquid petroleum gas could be applied for the reduction of  $\text{SnO}_2$ . As a first step, we are currently working on the optimization of the MR of  $\text{SnO}_2$  and the utilization of liquid natural gas for  $\text{SnO}_2$  reduction. The relevant results will be reported in due course.

## Conclusions

We studied the mechanism of a novel MR of  $\text{SnO}_2$  which is a clean, environmentally friendly reduction method for  $\text{SnO}_2$ . DFT calculations and thermodynamic simulations show that the carbon and hydrogen of  $\text{CH}_4$  bound to the surface of  $\text{SnO}_2$  independently and sequentially reduce  $\text{SnO}_2$ . Various gas-phase products, such as  $\text{H}_2\text{O}$ ,  $\text{CO}$ ,  $\text{CO}_2$ , and  $\text{H}_2$ , were produced from the early phase of reduction. The relative composition of the gas-phase product varies as a function of the amount of supplied  $\text{CH}_4$  and the temperature. In the early phase of the MR of  $\text{SnO}_2$  (low-temperature or less than  $R = 0.62$  of supplied  $\text{CH}_4$ ), hydrogen acts as a dominant reducer. As the supplied  $\text{CH}_4$  increases, the carbon from  $\text{CH}_4$  aggressively takes the oxygen from  $\text{H}_2\text{O}$  and  $\text{CO}_2$  forming  $\text{CO}$ . Hydrogen from  $\text{CH}_4$  and  $\text{H}_2\text{O}$  is released as  $\text{H}_2$ . The optimized operating condition of  $1,000^\circ\text{C}$  and  $R = 2.0$  was suggested from thermodynamic simulation data.

The reliability of this method was confirmed using an experimental batch test performed at  $1,000^\circ\text{C}$ . The high recovery of our MR of  $\text{SnO}_2$  (approximately 80%) and the high purity (99.34%) of the reduced Sn demonstrate the novelty of our method.

Our results demonstrate a novel MR method for  $\text{SnO}_2$  as an efficient and green method for recovery of Sn from  $\text{SnO}_2$ . In addition to the reduced metallic Sn, only several gas phase molecules and solid carbon were produced. The  $\text{H}_2/\text{CO}$  ratio in the gas-phase product was controllable by the amount of  $\text{CH}_4$  supplied and the operating

temperature. Our results open new avenues for the efficient and economic recovery of highly demanded metallic elements from complex oxide wastes, for example, the recovery of In and Sn from indium-tin oxide.

## Methods

**Thermodynamic simulations.** Thermodynamic simulations were performed with the HSC 6.0 code (Outotec Research, [www.hsc-chemistry.com](http://www.hsc-chemistry.com)). The relative thermodynamic stability of various Sn, C, O, and H chemical compounds was estimated at temperatures between 0 °C and 1,500 °C. For the initial equilibrium simulation, a mole of SnO<sub>2</sub> was balanced with continuously increasing CH<sub>4</sub> from 0 to 5 moles to clarify the effect of the SnO<sub>2</sub>/CH<sub>4</sub> ratio (R) on the relative amount of the final products.

**Density functional theory calculations.** Quantum chemical DFT calculations were performed with the VASP code<sup>59</sup>. A 3 × 2 × 4 rutile (110) and a 2 × 3 × 5 (100) supercells were used for surface reaction calculations and the most bottom triple layer was fixed during the optimization to ensure the structural robustness of the slab models (refer to Figure S2 for supercell geometry). Electron exchange and correlation were modeled using the Perdew-Burke-Ernzerhof (PBE)<sup>60</sup> functional and the interaction between the ionic cores and the valence electrons was described with the projector augmented-wave method<sup>61</sup>. The valence-electron wave functions were expanded in the plane-wave basis set up to the energy cutoff of 400 eV. The convergence criteria for the electronic structure and the atomic geometry were 10<sup>-4</sup> eV and 0.03 eV/Å, respectively.

**Experimental procedure.** A high purity SnO<sub>2</sub> electrode, which was previously used in glass-producing electric furnaces<sup>32</sup>, was acquired from Corning precision materials (Gumi, Korea). The average particle diameter of SnO<sub>2</sub> powders was 135 μm (Figure S3). For the laboratory scale MR of SnO<sub>2</sub> experiments, an alumina boat was loaded with 25 g of SnO<sub>2</sub> powder and exposed to a stream of CH<sub>4</sub> and Ar for 1 hour at 1000 °C. The CH<sub>4</sub> flow rate was 250 sccm. The molar ratio of the total supplied CH<sub>4</sub> was 1.85 to SnO<sub>2</sub>. The gas-phase concentration and composition of the reduced Sn was analyzed using gas chromatography (GC) and induced coupled plasma (ICP).

**Data availability.** The datasets generated during and/or analyzed during the current study are available from the corresponding author on reasonable request.

## References

1. Photos, E. The question of meteoritic versus smelted nickel-rich iron: Archaeological evidence and experimental results. *World Archaeol.* **20**, 403–421 (1989).
2. Needham, S. P., Leese, M. N., Hook, D. R. & Hughes, M. J. Developments in the Early Bronze Age metallurgy of southern Britain. *World Archaeol.* **20**, 383–402 (1989).
3. Roberts, B. Creating traditions and shaping technologies: understanding the earliest metal objects and metal production in Western Europe. *World Archaeol.* **40**, 354–372 (2008).
4. Radiivojević, M. *et al.* On the origins of extractive metallurgy: new evidence from Europe. *J. Archaeol. Sci.* **37**, 2775–2787 (2010).
5. Schmidt, P. & Avery, D. H. Complex Iron Smelting and Prehistoric Culture in Tanzania. *Science* **201**, 1085 (1978).
6. Kang, H. N., Lee, J.-Y. & Kim, J.-Y. Recovery of indium from etching waste by solvent extraction and electrolytic refining. *Hydrometallurgy* **110**, 120–127 (2011).
7. Rimaszeki, G., Kulcsar, T. & Kekesi, T. Application of HCl solutions for recovering the high purity metal from tin scrap by electrorefining. *Hydrometallurgy* **125**, 55–63 (2012).
8. Jun, W. S., Yun, P. S. & Lee, E. C. Leaching behavior of tin from Sn-Fe alloys in sodium hydroxide solutions. *Hydrometallurgy* **73**, 71–80 (2004).
9. Kim, S.-K., Lee, J.-C. & Yoo, K. Leaching of tin from waste Pb-free solder in hydrochloric acid solution with stannic chloride. *Hydrometallurgy* **165**, 143–147 (2016).
10. Lee, M.-S., Ahn, J.-G. & Ahn, J.-W. Recovery of copper, tin and lead from the spent nitric etching solutions of printed circuit board and regeneration of the etching solution. *Hydrometallurgy* **70**, 23–29 (2003).
11. Little, P. & Martin, M. H. A survey of zinc, lead and cadmium in soil and natural vegetation around a smelting complex. *Environ. Pollut.* (1970) **3**, 241–254 (1972).
12. Itoh, S. & Maruyama, K. *High Temp. Mater. Processes* **30**, 317–322 (2011).
13. Rabah, M. A. Combined hydro-pyrometallurgical method for the recovery of high lead/tin/bronze alloy from industrial scrap. *Hydrometallurgy* **47**, 281–295 (1998).
14. Sriprya, R. & Murty, C. V. G. K. Recovery of metal from slag/mixed metal generated in ferroalloy plants—a case study. *Int. J. Miner. Process.* **75**, 123–134 (2005).
15. Mitchell, A. R. & Parker, R. H. The reduction of SnO<sub>2</sub> and Fe<sub>2</sub>O<sub>3</sub> by solid carbon. *Miner. Eng.* **1**, 53–66 (1988).
16. Li, Y., Liu, Z., Li, Q., Liu, Z. & Zeng, L. Recovery of indium from used indium–tin oxide (ITO) targets. *Hydrometallurgy* **105**, 207–212 (2011).
17. Gupta, B., Mudhar, N. & Singh, I. Separations and recovery of indium and gallium using bis(2,4,4-trimethylpentyl)phosphinic acid (Cyanex 272). *Sep. Purif. Technol.* **57**, 294–303 (2007).
18. Thoburn, J. T. *Tin in the world economy*. (Edinburgh University Press, 1994).
19. François Hennart, J. Upstream vertical integration in the aluminum and tin industries. *J. Econ. Behav. Organ.* **9**, 281–299 (1988).
20. <https://www.itri.co.uk/sustainability/news-5/itri-survey-tin-demand-growing-slowly>.
21. <https://www.itri.co.uk/information/tinplate/general/tin-for-tomorrow-contributing-to-global-sustainable-development>.
22. <https://www.itri.co.uk/market-analysis/consumption/itri-survey-shows-tin-use-stable-to-slightly-stronger-in-> (2016).
23. Bae, J.-Y., Park, J., Kim, H. Y., Kim, H.-S. & Park, J.-S. Facile Route to the Controlled Synthesis of Tetragonal and Orthorhombic SnO<sub>2</sub> Films by Mist Chemical Vapor Deposition. *ACS Appl. Mater. Inter.* **7**, 12074–12079 (2015).
24. Snaith, H. J. & Ducati, C. SnO<sub>2</sub>-Based Dye-Sensitized Hybrid Solar Cells Exhibiting Near Unity Absorbed Photon-to-Electron Conversion Efficiency. *Nano Lett.* **10**, 1259–1265 (2010).
25. Vilà, A., Gomez, A., Portilla, L. & Morante, J. R. Influence of In and Ga additives onto SnO<sub>2</sub> inkjet-printed semiconductor. *Thin Solid Films* **553**, 118–122 (2014).
26. Kim, H. *et al.* Electrical, optical, and structural properties of indium–tin–oxide thin films for organic light-emitting devices. *J. Appl. Phys.* **86**, 6451–6461 (1999).
27. Bai, S. *et al.* Synthesis of SnO<sub>2</sub>–CuO heterojunction using electrospinning and application in detecting of CO. *Sens. Actuators, B* **226**, 96–103 (2016).

28. Suehle, J. S., Cavicchi, R. E., Gaitan, M. & Semancik, S. Tin oxide gas sensor fabricated using CMOS micro-hotplates and *in-situ* processing. *IEEE Electron Device Lett.* **14**, 118–120 (1993).
29. Nayral, C. *et al.* A Novel Mechanism for the Synthesis of Tin/Tin Oxide Nanoparticles of Low Size Dispersion and of Nanostructured SnO<sub>2</sub> for the Sensitive Layers of Gas Sensors. *Adv. Mater.* **11**, 61–63 (1999).
30. Dattoli, E. N., Davydov, A. V. & Benkstein, K. D. Tin oxide nanowire sensor with integrated temperature and gate control for multi-gas recognition. *Nanoscale* **4**, 1760–1769 (2012).
31. Bickerstaff, K. & B. P. L. A. Manufacture of flat glass. US patents: US2911759A (1959).
32. Citti, O., Williams, J. A. A. & McGarry, C. N. Tin oxide material with improved electrical properties for glass melting. US Patents: US7685843B2, (2010).
33. Fourcade, J. & Citti, O. In *73rd Conference on Glass Problems* 183–199 (John Wiley & Sons, Inc., 2013).
34. Betz, U., Kharrazi Olsson, M., Marthy, J., Escolá, M. F. & Atamny, F. Thin films engineering of indium tin oxide: Large area flat panel displays application. *Surf. Coat. Technol.* **200**, 5751–5759 (2006).
35. Ginley, D. S. & Bright, C. Transparent conducting oxides. *MRS Bull.* **25**, 15–18 (2000).
36. Nah, J.-W., Kim, J. H., Lee, H. M. & Paik, K.-W. Electromigration in flip chip solder bump of 97Pb–3Sn/37Pb–63Sn combination structure. *Acta Mater.* **52**, 129–136 (2004).
37. Cho, M. G., Kim, H. Y., Seo, S.-K. & Lee, H. M. Enhancement of heterogeneous nucleation of  $\beta$ -Sn phases in Sn-rich solders by adding minor alloying elements with hexagonal closed packed structures. *Appl. Phys. Lett.* **95**, 021905 (2009).
38. <https://www.lme.com>.
39. <https://www.itri.co.uk/sustainability/material-flow-and-recycling>.
40. Khoshandam, B., Jamshidi, E. & Kumar, R. Reduction of cobalt oxide with methane. *Metall. Mater. Trans. B* **35**, 825–828 (2004).
41. Ale Ebrahim, H. & Jamshidi, E. Kinetic Study of Zinc Oxide Reduction by Methane. *Chem. Eng. Res. Des.* **79**, 62–70 (2001).
42. Cetinkaya, S. & Eroglu, S. Thermodynamic analysis and reduction of tin oxide with methane. *Int. J. Miner. Process.* **110**, 71–73 (2012).
43. Cetinkaya, S. & Eroglu, S. Thermodynamic analysis and reduction of tungsten trioxide using methane. *Int. J. Refract. Met. Hard Mater.* **51**, 137–140 (2015).
44. Lee, T.-H. *et al.* Reduction Kinetics of Zinc Powder from Brass Converter Slag by Pyrometallurgical Method Using Hydrogen Gas. *KONA Powder Part. J.* **33**, 278–286 (2016).
45. Altay, M. C. & Eroglu, S. Isothermal Reaction of NiO Powder with Undiluted CH<sub>4</sub> at 1000 K to 1300 K (727°C to 1027°C). *Metal. Mater. Trans. B* **48**, 2067–2076 (2017).
46. Ale Ebrahim, H. & Jamshidi, E. Effect of mass transfer and bulk flow on the zinc oxide reduction by methane. *Ind. Eng. Chem. Res.* **41**, 2630–2636 (2002).
47. Ale Ebrahim, H. & Jamshidi, E. Kinetic Study and Mathematical Modeling of the Reduction of ZnO–PbO Mixtures by Methane. *Ind. Eng. Chem. Res.* **44**, 495–504 (2005).
48. Ng, K. S. *et al.* A multilevel sustainability analysis of zinc recovery from wastes. *Resour. Conserv. Recy.* **113**, 88–105 (2016).
49. Cetinkaya, S. & Eroglu, S. A Single-Step Process for Direct Reduction of Iron Oxide to Sponge Iron by Undiluted Methane. *JOM* **69**, 993–998 (2017).
50. Kim, H. Y., Park, J. N., Henkelman, G. & Kim, J. M. Design of a Highly Nanodispersed Pd–MgO/SiO<sub>2</sub> Composite Catalyst with Multifunctional Activity for CH<sub>4</sub> Reforming. *ChemSusChem* **5**, 1474–1481 (2012).
51. Van Hook, J. P. Methane–Steam Reforming. *Catal. Rev.* **21**, 1–51 (1980).
52. Bradford, M. C. J. & Vannice, M. A. CO<sub>2</sub> Reforming of CH<sub>4</sub>. *Catal. Rev.* **41**, 1–42 (1999).
53. Fan, M.-S., Abdullah, A. Z. & Bhatia, S. Catalytic Technology for Carbon Dioxide Reforming of Methane to Synthesis Gas. *ChemCatChem* **1**, 192–208 (2009).
54. Pakhare, D. & Spivey, J. A review of dry (CO<sub>2</sub>) reforming of methane over noble metal catalysts. *Chem. Soc. Rev.* **43**, 7813–7837 (2014).
55. Wang, S., Lu, G. Q. & Millar, G. J. Carbon Dioxide Reforming of Methane To Produce Synthesis Gas over Metal-Supported Catalysts: State of the Art. *Energy Fuels* **10**, 896–904 (1996).
56. Abánades, A. *et al.* Development of methane decarbonisation based on liquid metal technology for CO<sub>2</sub>-free production of hydrogen. *Int. J. Hydrogen Energy* **41**, 8159–8167 (2016).
57. Geißler, T. *et al.* Hydrogen production via methane pyrolysis in a liquid metal bubble column reactor with a packed bed. *Chem. Eng. J.* **299**, 192–200 (2016).
58. Van Der Laan, G. P. & Beenackers, A. A. C. M. Kinetics and Selectivity of the Fischer–Tropsch Synthesis: A Literature Review. *Catal. Rev.* **41**, 255–318 (1999).
59. Kresse, G. & Furthmüller, J. Efficiency of ab-initio total energy calculations for metals and semiconductors using a plane-wave basis set. *Comput. Mater. Sci.* **6**, 15–50 (1996).
60. Perdew, J. P., Burke, K. & Ernzerhof, M. Generalized gradient approximation made simple. *Phys. Rev. Lett.* **77**, 3865–3868 (1996).
61. Blochl, P. E. Projector Augmented-Wave Method. *Phys. Rev. B* **50**, 17953–17979 (1994).

## Acknowledgements

This work was supported by the Korea Institute of Energy Technology Evaluation and Planning (KETEP) and the Ministry of Trade, Industry & Energy (MOTIE) of the Republic of Korea (No. 20155020101050). This research used resources of the Center for Functional Nanomaterials, which is a U.S. DOE Office of Science Facility, at Brookhaven National Laboratory under Contract No. DE-SC0012704. Computing time was provided by the National Institute of Supercomputing and Network/Korea Institute of Science and Technology Information (KSC-2016-C3-0037).

## Author Contributions

H.Y.K., J.H.H., and S.-R.L. designed this work. H.H., M.Y., H.A., and K.S. performed thermodynamic simulations and DFT calculations. T.H., Y.S., and S.K. carried out the experiments. H.Y.K. wrote the manuscript. All the authors contributed to discuss on the manuscript.

## Additional Information

**Supplementary information** accompanies this paper at <https://doi.org/10.1038/s41598-017-14826-7>.

**Competing Interests:** The authors declare that they have no competing interests.

**Publisher's note:** Springer Nature remains neutral with regard to jurisdictional claims in published maps and institutional affiliations.





**Open Access** This article is licensed under a Creative Commons Attribution 4.0 International License, which permits use, sharing, adaptation, distribution and reproduction in any medium or format, as long as you give appropriate credit to the original author(s) and the source, provide a link to the Creative Commons license, and indicate if changes were made. The images or other third party material in this article are included in the article's Creative Commons license, unless indicated otherwise in a credit line to the material. If material is not included in the article's Creative Commons license and your intended use is not permitted by statutory regulation or exceeds the permitted use, you will need to obtain permission directly from the copyright holder. To view a copy of this license, visit <http://creativecommons.org/licenses/by/4.0/>.

© The Author(s) 2017